THE SPECTRAL IRRADIANCE OF THE MOON

HUGH H. KIEFFER[1,2] AND THOMAS C. STONE
US Geological Survey, 2255 North Gemini Drive, Flagstaff, AZ 86001

ABSTRACT

Images of the Moon at 32 wavelengths from 350 to 2450 nm have been obtained from a dedicated observatory during the bright half of each month over a period of several years. The ultimate goal is to develop a spectral radiance model of the Moon with an angular resolution and radiometric accuracy appropriate for calibration of Earth-orbiting spacecraft. An empirical model of irradiance has been developed that treats phase and libration explicitly, with absolute scale founded on the spectra of the star Vega and returned *Apollo* samples. A selected set of 190 standard stars are observed regularly to provide nightly extinction correction and long-term calibration of the observations. The extinction model is wavelength-coupled and based on the absorption coefficients of a number of gases and aerosols. The empirical irradiance model has the same form at each wavelength, with 18 coefficients, eight of which are constant across wavelength, for a total of 328 coefficients. Over 1000 lunar observations are fitted at each wavelength; the average residual is less than 1%. The irradiance model is actively being used in lunar calibration of several spacecraft instruments and can track sensor response changes at the 0.1% level.

Key words: methods: miscellaneous — Moon — techniques: photometric

1. INTRODUCTION: PURPOSE AND USE

Although the Moon is our closest celestial neighbor, there have been surprisingly few studies to characterize its absolute brightness with regard to surface spatial variegation, spectral content, and variation with illumination geometry. A program for precision radiometry of the Moon was established to address a critical need of programs for Earth remote sensing from space: determination of the long-term stability of the sensor's measurements on-orbit. This requires periodic in-flight calibration by viewing a multispectral standard. On-board calibration systems for imaging instruments are designed for the greatest stability practical, but drifts of 1% to several percent over a 5 year lifetime appear to represent the current limitations (Gellman et al. 1993; Ohring et al. 2004). Among these calibration systems, solar diffusers maintain the color temperature and spectral fine structure of sunlight; however, they are susceptible to changes in their reflectance properties from exposure to the near-Earth space environment or from contamination. Serious efforts to understand and minimize the effects of these changes to in-flight sensor calibration have been made for several recent instruments (see, e.g., Bruegge et al. 1996; Guenther et al. 1996; Folkman et al. 2001; Alhajjah et al. 2004).

Use of the Moon to address in-flight calibration was suggested nearly 20 years ago (Kieffer & Wildey 1985, 1996; Pugacheva et al. 1993), and a NASA-sponsored project to accurately determine the irradiance and radiance of the Moon began routine operations in 1996 (Kieffer & Anderson 1998; Anderson & Kieffer 1999; Stone & Kieffer 2002).

The surface of the Moon has reflectance properties that are virtually invariant over time (Kieffer 1997). However, the Moon's brightness varies in a complex way as a result of the spatial variegation of lunar albedo, the physical and optical libration over periods of a month, a year, and 18 years, and the strong dependence on phase angle of the surface photometric function. Yet, the intrinsic stability of the lunar surface photometric properties means that a lunar radiometric model, once established, can be applied to spacecraft observations made at any time, including retroactively. A corollary is that observations of the Moon made by the same or different instruments at diverse times can be compared through use of a lunar radiometric model.

Advantages of using the Moon as a calibration source include the following: the reflectance properties of the "diffuser" are stable to the order of 10^{-8} yr^{-1} (Kieffer 1997); the target has a sharp edge (for at least half of its circumference); the radiance of the background surrounding the target is virtually zero (a 4 K blackbody, plus stars); the target is spectrally bland (slightly red, with two weak, broad bands over the visible and near-infrared); and the target is accessible to all spacecraft, with similar geometry every month. Disadvantages include the following: the flux from the lunar surface covers roughly one-fourth the dynamic range of most bands of satellite instruments that view the Earth's land surface at solar reflectance wavelengths; the target is spatially variegated; the target brightness has a strong dependence on phase angle; and the target exhibits librations of about ±7°. All but the dynamic range issue are being addressed by the RObotic Lunar Observatory (ROLO; Kieffer & Wildey 1996) program at the US Geological Survey (USGS) in Flagstaff, Arizona, through development of the ROLO lunar model (Anderson et al. 2001; Stone et al. 2002; Stone & Kieffer 2002). The ROLO facility was designed for and is dedicated to radiometric observations of the Moon. The instrumentation and control system are described in Anderson et al. (1999).

1.1. *Prior Irradiance Work*

Irradiance observations of the unresolved Moon covering a wide range of phase angles were made in the *UBV* and nine narrower bands covering 359–1064 nm by Lane & Irvine (1973), who report 33 observations over 29 nights covering all but two lunations from 1964 July to 1965 November. That paper is a landmark in absolute photometry of the Moon and cites virtually all work through 1970. Their work was a major

---

improvement over prior irradiance observations and represents the last comprehensive observation database prior to the ROLO project. Lane & Irvine (1973) modeled their observations of astronomic magnitude to be linear with phase angles smaller than $40°$ and cubic at larger angles; the standard deviation of the residuals for a band was typically 0.05, "giving an estimate of the accuracy of the curves." They found that the Moon becomes redder with increasing phase angle, similar to some earlier observations. However, their work does not cover the opposition effect or libration; their stated phase coefficient uncertainties are $\sim 0.1\%$ deg^{-1}, roughly an order of magnitude larger than for the ROLO model (see § 4.1).

Earth-based observations of lunar photometric properties are limited to phase angles larger than about $1°5$: the onset of eclipse phenomena. However, Moon-orbiting spacecraft observations have allowed study of the opposition effect to virtually $0°$, enabling determination of the opposition effect to small angles and sparking vigorous debate over its cause (see § 3.3).

1.1.1. Polarization

It has long been known that light from the Moon is linearly polarized and that this polarization decreases with increasing albedo (Umov 1905; Dollfus 1962, p. 131; 1998). Near 325 nm at small phase angles it is negative, with an extreme of -1.2% at about $12°$ (Dollfus 1961, p. 343). Polarization passes through zero near $24°$ and reaches a maximum of $\sim 8\%$ near $90°$ phase in the UV (Lyot 1929). In polarization measurements of 14 lunar regions at eight wavelengths from 327 to 1050 nm, Dollfus & Bowell (1971) found that the maximum polarization P_m (in percent) closely followed the relation $\ln P_m = -(1.81 + \ln A_n)/0.724$, where A_n is the normal albedo, i.e., the reflectance at zero incidence and emission angles.

1.2. Application to Spacecraft Calibration

Current knowledge of lunar photometry resulting from the ROLO program is adequate to support precise determination of the responsivity history of imaging instruments in orbit around the Earth. The spatially integrated radiance derived from the nominal calibration of spacecraft lunar images can be compared directly with models of the lunar irradiance to determine instrument gain factors. Descriptions of the lunar calibration technique applied to spacecraft can be found in the literature (e.g., Barnes et al. 2001, 2004; Kieffer et al. 1999, 2002).

Most observations of the Moon utilizing the nominal nadir-viewing capability of spacecraft have been made with the Moon within a few days of full. Typically, low- to moderate-altitude Earth-orbiting spacecraft instruments will view the Moon using an attitude maneuver that allows the instrument to scan past the Moon in a manner similar to acquisition of a terrestrial scene, acquiring all bands simultaneously. Spatial resolution ranges from 6 to >1000 pixels across the diameter of the Moon. Some instruments in near-polar orbit have "space-view" ports nearly perpendicular to the plane of the orbit; the Moon can be viewed through such a port once per month without a spacecraft attitude maneuver. Geosynchronous meteorological satellites commonly have a square field of regard; the Moon periodically appears in the corners of such images, allowing its use for calibration without need for a maneuver.

The Moon is available to all Earth-orbiting spacecraft at least once per month, and thus it can be used to tie together the at-sensor radiance scales of all instruments participating in lunar calibration without requiring near-simultaneous observations.

A corollary, resulting from the intrinsic stability of the lunar surface, is that any future improvements to radiometric knowledge of the Moon could be applied retroactively to instrument calibration.

2. OBSERVATIONAL PROGRAM

The ROLO specification of lunar spectral irradiance is founded on a database of spatially resolved radiance images of the Moon acquired from a ground-based observatory, designed and built specifically for the project. ROLO observational data were collected for more than 6 years, spanning phase angles from near eclipse to typically $90°$ before and after full Moon and covering a wide range of the observable libration angles. Of this time, more than 3 years had all 32 bands observed and reduced for the current analysis.

2.1. Observatory Facility

The ROLO observatory is located on the campus of the USGS field center in Flagstaff, Arizona (lat. N$32°12'52''9$, long. W$111°38'5''0$, alt. 2148 m). Although the site is on the edge of the city, sky brightness has not been a problem because observations are of relatively bright objects (the Moon, and stars of magnitude lower than 6), and the use of imaging arrays allows for a detailed sky correction on each image. The observatory building has a roll-off roof to allow rapid access to the entire sky all night.

2.1.1. Telescope Systems

Two nearly identical telescopes are mounted straddling the ring of a fork equatorial mount. The telescopes are Ritchey-Chrétien design with 8 inch (20 cm) diameter primary mirrors. The focal length for each telescope is set to allow an image of the Moon at perigee to fall entirely within its detector array, close to 1 m for both. The brightness difference between the Moon and stars is accommodated by inserting a neutral density filter into the optical path for lunar observations; stars are observed through a fused silica glass compensator. The optical systems are entirely on-axis, with no diagonal reflections, and hence are insensitive to polarization.

Wavelength coverage is the solar-reflectance range of Earth-observing data products: 350–2500 nm. Two types of detectors are used: the Visible–Near Infrared (VNIR) camera is a 512 pixel square silicon CCD maintained at $-45°$C by a thermoelectric cooler, and the Shortwave Infrared (SWIR) camera is a liquid nitrogen–cooled, 256 pixel square HgCdTe array detector nearly identical to the NICMOS detector on the *Hubble Space Telescope*. Apart from occasional maintenance, both detectors are kept cold continuously.

The image data acquisition system is virtually fully automated (Anderson et al. 1999). At the start of each observing night a master computer program first queries an ephemeris program (MICA)[3] to determine the positions of targets, then generates the observation sequence for the entire night, including hardware settings and camera exposure times for each target and filter. The master computer communicates with two separate computers that control the cameras and record the image data and a third that slews the telescope mount. All image data and ancillary pointing parameters are transferred to a separate computer at the end of the night for archiving onto CD-ROM media.

---

[3] Multiyear Interactive Computer Almanac: 1990–2005, from the US Naval Observatory, http://aa.usno.navy.mil/software/mica/micainfo.html.

2.1.2. *Band Filters*

The 23 VNIR and nine SWIR passbands used in the ROLO system are diagrammed in Figure 1. These bands include several commonly found in terrestrial remote sensing applications and also traditional stellar photometry bands, but with two spectrally adjacent filters to resolve color trends within these photometry bands. A listing of the effective wavelengths, widths, and uses is given in Table 1.

Effective wavelength is defined by

$$\lambda_{\mathrm{eff}} \equiv \frac{\int_{\lambda_1}^{\lambda_2} \lambda L_\lambda R_b(\lambda)\, d\lambda}{\int_{\lambda_1}^{\lambda_2} L_\lambda R_b(\lambda)\, d\lambda}, \tag{1}$$

where L_λ is a particular radiance spectrum and R_b is the spectral responsivity of a particular band. For "white," L_λ is unity; for solar and lunar effective wavelengths L_λ is the solar spectrum and the solar spectrum times lunar reflectance, respectively. For lunar effective wavelengths, calculation of equation (1) is iterated using the model-fitted determination of lunar reflectance (see § 3.3) until changes are negligible. It is noteworthy that because of the general redness of the Moon, the effective wavelengths for solar and lunar radiation are increasingly different as bandwidth increases.

All the filters are multilayer interference filters. The spectral transmission was measured for each, either by the manufacturer or by the Center for Remote Sensing at the University of Arizona, under laboratory ambient conditions with nearly collimated light normal to the filter. For the SWIR filters, the wavelength shift in operating at liquid nitrogen temperature was computed by the manufacturer. For each filter, the spectral transmission for the ROLO optical configuration was computed by convolving the measured filter response with a nominal formula for off-axis wavelength shift, weighted by the solid angle of the ROLO Cassegrain telescope feed.

2.2. *Lunar and Stellar Image Database*

Routine data acquisitions by ROLO began in 1996 March with the VNIR camera only; the SWIR camera came online in 1998 January. Observations ceased in 2003 September with the expiration of funding for operations. During normal operations, the Moon was observed every clear night from first quarter to last quarter lunar phase. Lunar images were acquired in all 32 bandpass filters approximately every half-hour when the Moon was higher than 30° above the horizon. The remainder of the observing time (~75% when the Moon was accessible and full time otherwise) was dedicated to stellar observations for use in determining atmospheric extinction and instrument absolute response. Stellar targets were a subset of 190 "standard" stars selected by the ROLO project specifically for their invariant properties. The same stars were imaged repeatedly through the night.

The database currently contains over 85,000 individual images of the Moon and several hundred thousand star images. Copies of the at-telescope images and ancillary telescope data are maintained for public access at the Earth Sciences DAAC at the NASA Goddard Space Flight Center. The primary archive of raw and processed data is kept at the USGS Flagstaff Science Center.

Figure 2 shows coverage in phase and libration angles for ROLO data processed through 2001 March (67,505 images). Although spanning not quite 1/4 of the 18 yr lunar phase/libration cycle (Saros cycle), the libration space is substantially filled.
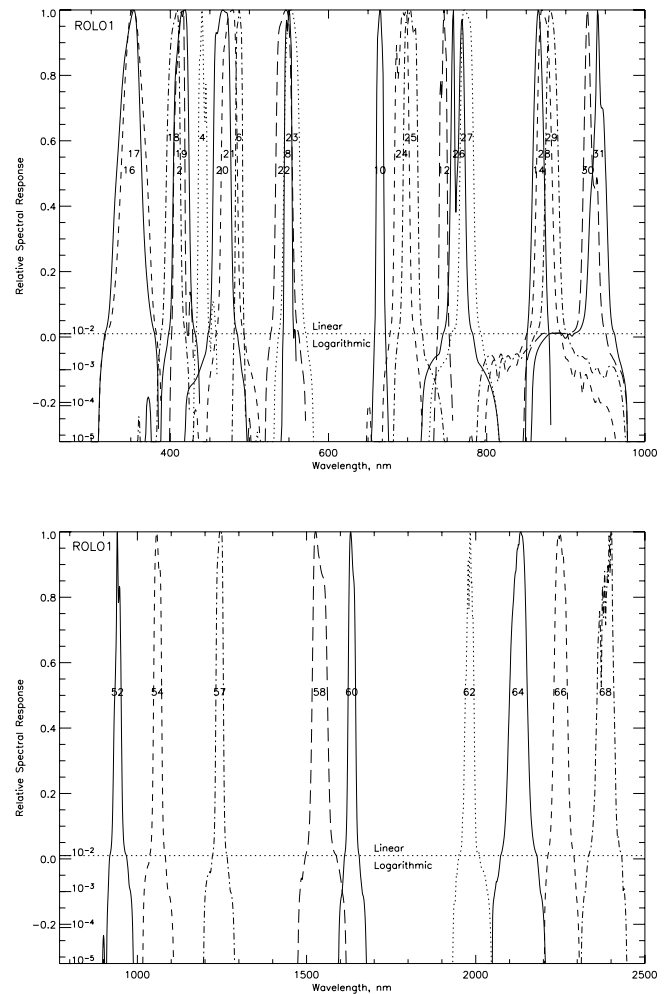

Fig. 1.—Spectral response of the ROLO bands, normalized to 1.0 maximum. The ordinate is linear in the upper portion of the plot in order to display the shape of the primary response. In the lower portion, the wings are displayed on a logarithmic scale. Outside of responses above 0.002, the raw measurement values have been filtered with a Gaussian of $\sigma = 8$ nm. The integers near half-maximum response are the ROLO filter numbers.

However, within narrow ranges of phase angles (roughly parallel arrows in the figure), libration coverage is sparse. The cumulative histogram of Figure 2 (*bottom*) shows that the distribution in phase angles is fairly even.

2.3. *Data Reduction*

A general description of the ROLO data reduction system is found in Stone et al. (2002). Additional details describing three of the more important elements are given here.

2.3.1. *Atmospheric Extinction Model*

Nightly extinction measurements of stars are used to develop a time-dependent characterization of the atmosphere, which is used to specify extinction for the lunar images. The method follows the approach of Hayes & Latham (1975), building up a total absorption profile from multiple discrete atmospheric constituents. The ROLO implementation treats the extinction coefficient for each component as a product of a spectral coefficient, a time-dependent column abundance, and the slant path length.

Each star image is reduced to an at-telescope irradiance and converted to magnitude, and the set of observations for the

TABLE 1
ROLO Bands

Nominal Wavelength (nm)	Width (nm)	Use[a]	ROLO Filter ID	Effective Wavelength (nm)			Solar Flux (W m^{-2} nm^{-1})
				White	Sun	Moon	
VNIR							
347...	32.5	$u-$	16	348.48	349.51	351.19	0.9681
353...	31.6	$u+$	17	353.39	354.59	356.39	0.9938
405...	16.2	$v-$	18	404.06	404.91	405.27	1.5517
413...	12.5	C	2	412.16	412.29	412.52	1.7080
415...	17.8	$v+$	19	414.14	414.31	414.64	1.7031
442...	9.6	C	4	441.31	441.61	441.74	1.8443
467...	20.0	$b-$	20	465.62	465.71	465.86	2.0162
476...	18.4	$b+$	21	474.86	474.91	474.90	2.0007
488...	7.9	C	6	486.91	486.89	486.89	1.9172
545...	18.8	$y, V-$	22	543.93	543.99	544.05	1.8718
550...	8.7	C	8	549.07	549.10	549.10	1.8702
555...	18.1	$y, V+$	23	553.70	553.74	553.74	1.8575
667...	8.3	C	10	665.11	665.12	665.11	1.5456
695...	16.8	$R-$	24	693.13	693.08	693.02	1.4410
706...	16.7	$R+$	25	703.69	703.66	703.61	1.4038
747...	8.7	C	12	745.31	745.32	745.30	1.2767
766...	16.8	...	26	763.74	763.67	763.58	1.2255
777...	16.9	...	27	774.86	774.85	774.78	1.1966
868...	13.9	C	14	865.30	865.32	865.27	0.9689
875...	18.4	$I-$	28	872.61	872.64	872.56	0.9662
885...	16.0	$I+$	29	882.13	882.06	881.90	0.9589
935...	17.6	H_2O-	30	928.59	928.37	928.00	0.8273
944...	18.8	H_2O+	31	939.58	939.33	938.98	0.8042
SWIR							
944...	21.5	Comp	52	942.19	942.08	941.94	0.7981
1062...	27.1	Clear	54	1059.60	1059.49	1059.43	0.6521
1247...	23.3	C	57	1243.27	1243.23	1243.16	0.4740
1543...	48.6	C	58	1538.90	1538.61	1538.28	0.2788
1638...	23.4	C	60	1633.67	1633.61	1633.52	0.2394
1985...	38.5	H_2O	62	1981.63	1981.52	1981.33	0.1242
2132...	54.7	C	64	2126.78	2126.19	2125.54	0.0878
2256...	48.2	C	66	2250.83	2250.89	2250.66	0.0702
2390...	58.2	C	68	2384.06	2383.52	2383.15	0.0583

[a] Entries are as follows: (C) common spacecraft band; (other letters) astronomic photometry bands; (Comp) VNIR-SWIR comparison; (H_2O) water vapor absorption; (Clear) minimum atmospheric absorption.

entire night are processed as a system of linear equations describing the multiple-component extinction. For one observation in one band,

$$m_{\mathrm{obs}} = m_0 + \sum_{n=1}^{N}(k_n \rho_n X_{\mathrm{obs}}), \qquad (2)$$

where m_0 is the exoatmospheric magnitude and X is the air mass. The sum over n represents the atmospheric components, for which the relative abundances ρ_n are solved by least-squares fitting. The k_n-coefficients are developed from the nominal atmospheric transmission in each band, as described below. Input values m_{obs} are generated by a numerical aperture photometry routine that integrates the central maximum of a stellar image out to a specified radius and subtracts an integrated sky background annulus. Corrections for stellar point-spread functions, developed for each band by separate analysis, are applied to the background-subtracted integrations.

Atmospheric absorption is defined for seven components: "normal gases" (N_2, O_2, CO_2, and trace gases, plus Rayleigh

scattering), ozone, water vapor, and four aerosols. Transmission spectra for these components were computed using MODTRAN (Berk et al. 1989), version 3.7, for a vertical path from 2 to 100 km altitude, the 1976 US standard atmosphere, and midlatitude winter conditions (see Fig. 3). This represents the minimum extinction expected over Flagstaff, which is then scaled by the component abundances. The k_n-coefficients are computed by convolving the MODTRAN spectra with the ROLO instrument relative spectral response (RSR) functions for each wavelength band, weighted by representative stellar color spectra appropriate for the stars observed.

The atmospheric component abundances ρ_n are allowed to vary independently with time through the night, modeled by a second-order Chebyshev polynomial:

$$\rho_n = C_a + C_b t + C_c(2t^2 - 1), \qquad (3)$$

where the observation time t is represented by a linear mapping of the hours 00:00–15:00 UT (appropriate for Flagstaff) onto the interval $[-1, 1]$.
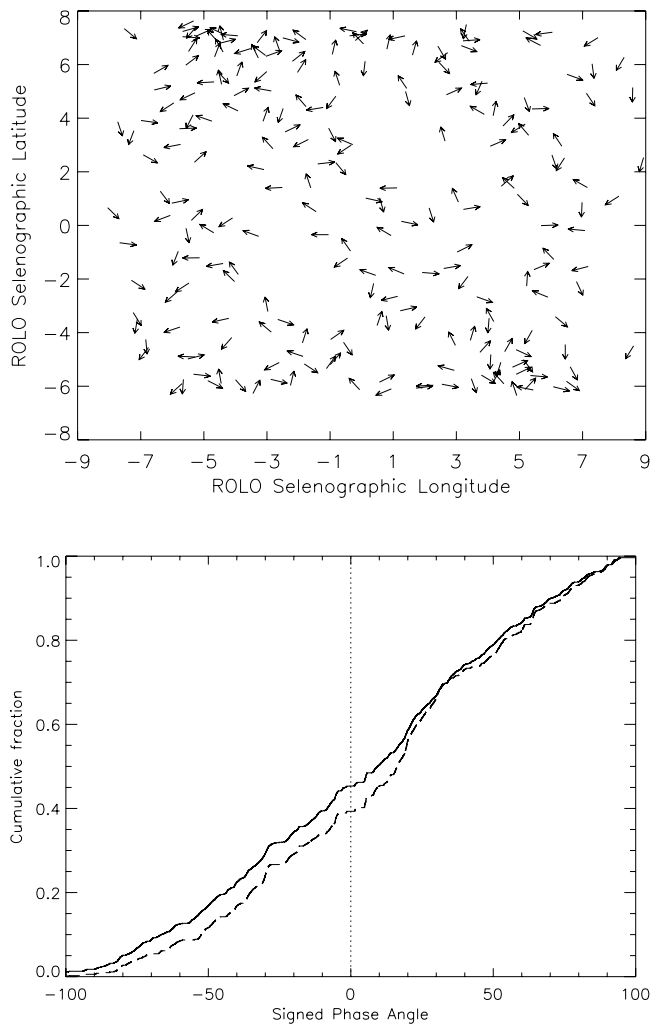
Fig. 3.—Spectra of the components of atmospheric extinction. Rayleigh scattering and the major gases, including 360 ppmv CO_2, are shown as the solid line "NormalGas." Water vapor and ozone are shown as the long-dashed line and dash-dotted line, respectively, and 4 μm radius cirrus is shown as the triple-dot-dashed line. Rural, volcanic, and tropospheric aerosols are shown as the shallow-sloped dotted, dashed, and solid lines, respectively.

Fig. 2.—Distribution of phase and libration angles in the ROLO observations. *Top*: Libration coverage through 2001 March. Phase angle is indicated by the direction of the arrows, with $0°$ shown as vertical up. Each point is an average for one night. *Bottom*: Cumulative histogram of phase angles for all 67,505 images (*solid line*) and for the 38,656 images in the 1208 sequences used for the irradiance model fit (*dashed line*; see § 3.3).

The system described by equations (2) and (3) has three free parameters for each of the seven atmospheric components, plus the exoatmospheric magnitude term, for each band. In practice, a time-dependent instrument gain term is included with m_0. ROLO observes ~12 different extinction stars typically $10–15$ times each night in all 32 filters. Solution of this system is handled by a modified gradient minimization algorithm that reduces the residuals along their gradients in parameter space to within a specified tolerance but not to their absolute minimum. Checks for a physically sound solution are performed prior to subsequent iterations. Utilizing this approach results in relatively rapid convergence, despite the large number of data points and free parameters. Results from the fit define the atmosphere in terms of the coefficients $C_{[a,b,c]}$ of equation (3); these are then used to generate extinction corrections for the acquisition times and air-mass values of the lunar images.

2.3.2. Radiance Calibration

Absolute calibration of the ROLO lunar radiance images has proceeded along several pathways and is undergoing continued refinement. The original project design used a near-field diffusing screen with a calibrated lamp; this system now is used
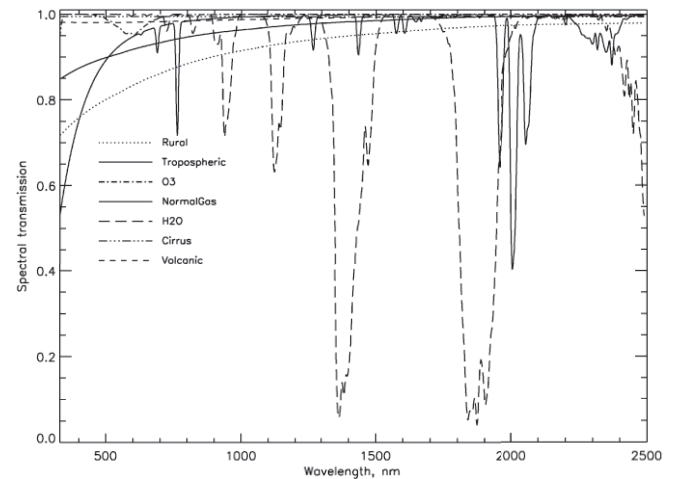
only to generate flat-fielding images. The radiance scale currently applied to ROLO observational data is derived from observations of Vega (α Lyr) by the ROLO telescopes and published absolute flux measurements. Vega is one of the ROLO standard stars, regularly observed when visible in the night sky. In a dedicated reprocessing of all observations through 2001 March that contained Vega, the ROLO atmospheric extinction algorithm was repeatedly iterated to cull lesser quality measurements and converge on the at-telescope Vega instrument magnitude (DN s^{-1}, where DN is detector counts) for each band. The absolute flux measurements of Hayes (1985) and Strecker et al. (1979) were used to scale a model stellar spectrum (Castelli & Kurucz 1994) for Vega. This spectrum was then convolved with the ROLO instrument RSR functions to give the effective photon fluxes in each band. The flux/DN rate ratios form the basis for the absolute calibration, modified by a model for long-term degradation of the telescope optics.

Short-term temporal instrument gain offsets affect the nightly radiometric measurements. The atmospheric extinction algorithm iterates to a solution for the exoatmospheric irradiance of the observed stars, with instrument gain included as an adjustable parameter. A subset of ROLO observations that include only the most stable extinction corrections is used to generate a table of exoatmospheric stellar irradiances for the ROLO standard stars. During times of the year when Vega is not visible, this table is used along with measurements of other photometric stars to anchor the instrument/atmospheric correction, thus giving a consistent absolute scale for the Moon.

Further analysis of the ROLO lunar irradiance specification has revealed the need for an absolute radiometric scale that does not depend on exoatmospheric sources. If a systematic bias were induced by the atmospheric correction algorithm, its effect on the Vega calibration observations would be canceled during calibration of the extinction-corrected lunar images. A dedicated effort is currently underway to tie the ROLO instrument response to the radiometric scale of the National Institute of Standards and Technology (NIST). The technique utilizes an on-axis collimated light source large enough to fill the field of view of the ROLO telescopes. The "artificial Moon" at the collimator prime focus has a primary calibration from NIST and receives repeated transfer calibrations against an NIST field-deployable

Fig. 4.—ROLO ALEX-projected image at 550 nm, phase angle 9°.02, selenographic subobserver longitude −2°.87, and latitude 6°.80. The white area surrounding the lunar disk is the accommodation for extremes in libration.

radiance source during periodic field campaigns at ROLO. Radiance images of the collimated source are compared against the prime-focus source radiance and convolved with the spectral reflectance of the collimator mirror (measured at NIST) and the ROLO system band spectral responses to develop the calibration. Results of this work are still preliminary; the improved radiance scale will be implemented in future versions of the ROLO lunar models and the radiance image data set.

2.3.3. Geometric Processing

The location and orientation of the Moon in the sky are computed for 20 minute intervals at the beginning of each night's observing session, then linearly interpolated in real time for each pointing to the Moon. The ephemeris is computed again during the data reduction processing for the actual time of acquisition. The location of the lunar disk in the digital image is determined by multiple measurements of the limb radius. Radial line segments are constructed from bilinear interpolation of the image pixels, and the disk edge is defined as the point of maximum intensity slope, found by parabolic interpolation over four 0.5 pixel radial elements. The number of measurements along the limb is on the order of the Moon radius in pixels. These measurements are iterated and the center point adjusted until the mean absolute deviation changes by a negligible amount.

The lunar images are resampled onto a uniform selenographic grid using bilinear interpolation. A projection was chosen that minimizes distortion of the raw image but allows coverage of all points on the Moon ever visible from the Earth; this is a modified Lambert azimuthal equal-area (ALEX) projection:

$$\alpha = P_2 \sin\left(\frac{\theta}{P_1}\right), \tag{4}$$

where α is the radial distance of the projected point from the center of the projection (corresponding to the [0, 0] point of the selenographic coordinate system), θ is the great-circle distance of a point from [0, 0], $P_1 = \theta_{max}/90°$, and P_2 is chosen to yield the desired resolution at the grid center. In addition, θ_{max} must be at least as large as the angle to the limb of the Moon for the extreme of topocentric libration; a value of $90° + 11°$ is used. The lunar radius is assumed to be 1737.4 km; the radius to the edge of the projection is 288 pixels for VNIR images and 144 for SWIR. Figure 4 shows an example of this ALEX projection.

3. LUNAR IRRADIANCE MODEL

3.1. The Irradiance Data Table and Initial Data Selection

The lunar irradiance is derived from integrations of ROLO lunar images that have been corrected for atmospheric extinction and calibrated to radiance:

$$I'_k = \Omega_p \sum_{i=1}^{N_p} L_{i,k}, \tag{5}$$

where $L_{i,k}$ is an individual radiance measurement (i.e., pixel) on the Moon in band k, Ω_p is the solid angle of 1 pixel, and N_p is the total number of pixels in the lunar disk image. Because the integrated lunar radiance in equation (5) covers the full lunar disk and because the Moon is viewed against a black background, I'_k functions as an irradiance and follows the "one-over-R-squared" law with respect to the Moon-viewer distance. In practice, the lunar image underfills the ROLO telescope detector arrays, and there is an edge of pixels around the image that view the black sky, even at lunar perigee.

The image irradiance values, along with formal estimates of uncertainty, instantaneous calibration values, observation times, geometric parameters, and the summed radiances for up to 11 small regions extracted from fixed square areas of the ALEX images (called "chips"), are placed in a large structured table of several data types called the "Alex table." Since these data are accessed a large number of times during model development, for efficiency they have been converted into a matched pair of integer and floating-point binary arrays; the Alex table contents are shown in Table 2.

ROLO has measured lunar radiances from the edge of eclipse to the lunar quarter phases whenever skies were clear. Some additional observations were made with less than half the visible Moon illuminated. The version 3 Alex table contains 67,505 individual lunar observations, with at least 2306 observations for each VNIR filter and at least 1463 observations for each SWIR filter. An initial parsing was done to retain only sequences that include all 32 filters exactly once, indicating that the series acquisition was normal. This yielded 1249 sequences of the 32 bands. These observations are distributed relatively uniformly over phase angle (see Fig. 2) but have some correlation with libration because the coverage was only about 1/4 of a Saros cycle. Nonetheless, these data should support modeling for phase angles from $1°.5$ to $90°$.

Associated with each observation are radiance sums for 11 small areas distributed across the Moon, described in Table 3. As a check on image quality, the radiances L_k for each chip for each band k were fitted by

$$L_k = \sum_{i=0}^{3} a_{ikm}\mu_0^i + \sum_{j=0}^{3} b_{jkm}\left(\frac{\mu_0}{\mu+\mu_0}\right)^j + h_{km}\left(\frac{\mu_0}{\mu+\mu_0}\right)e^{g/c_g}, \tag{6}$$

where m is the chip index, $\mu_0 = \cos$ (incidence angle), $\mu = \cos$ (emission angle), and g is the phase angle. Here, c_g is set to $8°.5$.

These fits constitute an additional quality test on images before the full irradiance fit through the following procedure: First, chips that are not illuminated (incidence angle $>88°$) or not visible (emission angle $>89°$) are omitted. For each image (sequence and band) processed, those chips with brightness $[L/(E_S/\pi)]$ greater than 0.01 are selected, and their fractional residuals (absolute fit residual divided by chip brightness) are averaged, weighted by the reciprocal of the uncertainty for that chip and image. Then the absolute values of these image averages are averaged over all bands in a sequence. Sequences with residuals greater than 7% are effectively eliminated by increasing their uncertainties by a factor of 100. The chip-fitting process is then repeated with the revised uncertainties. This two-pass procedure rejects about 40 sequences, including any in which otherwise undetected thin clouds may have partially obscured the Moon.

3.2. Conversion to Disk Reflectance

Although both the ROLO observations that form the basis of the lunar photometric model and spacecraft images of the Moon

are processed as radiance, the development of coefficients in the lunar irradiance model is done in dimensionless units of reflectance, that is, in albedo. The measured irradiance I' is reduced to the corresponding irradiance I at the standard distances adopted by ROLO: a Sun-Moon distance $D_{\text{S-M}}$ of 1 AU and a viewer-Moon distance $D_{\text{V-M}}$ of 384,400 km (the mean radius of the Moon's orbit around the Earth); thus,

$$I = f_d I', \;\; \text{where } f_d = \left(\frac{D_{\text{S-M}}}{1\,\text{AU}}\right)^2\left(\frac{D_{\text{V-M}}}{384,400\,\text{km}}\right)^2. \tag{7}$$

The conversion between irradiance and effective disk reflectance is

$$I_k = A_k \Omega_{\text{M}} E_k/\pi, \tag{8}$$

where A_k is the disk-equivalent albedo for band k, Ω_{M} is the solid angle of the Moon ($=6.4177\times10^{-5}$ sr), and E_k is the solar spectral irradiance at the effective wavelength $\lambda_{\text{S},k}$ of a band for solar radiation. The last two terms are both at standard distances. This conversion involves a solar spectral irradiance model, which may have significant uncertainties in some wavelength regions. However, the direct dependence on solar model cancels to first order as long as the same model is used in going from irradiance to reflectance and back. For physically based lunar photometric models, it is the absolute values of A that are important and thus would be influenced by errors in the solar spectral irradiance.

The solar irradiance in equation (8) is assumed constant for each band. For ROLO work, it is derived from the model of Wehrli (1986, pp. 119–126) and is calculated using

$$E_k = \frac{\int_{\lambda_1}^{\lambda_2} E_{\text{S}}(\lambda)R_k(\lambda)\,d\lambda}{\int_{\lambda_1}^{\lambda_2} R_k(\lambda)\,d\lambda}, \tag{9}$$

where $E_{\text{S}}(\lambda)$ is the Sun's spectral irradiance at 1 AU, $R_k(\lambda)$ is the system RSR for the band, and the limits for the integrals are the wavelengths over which the spectral response is measured. All work thus far has ignored the temporal variation of the solar spectral irradiance. The variation in total solar irradiance is about 0.2% (Fröhlich 2000), although it is considerably higher in the ultraviolet.

It is the disk reflectances A from the ROLO measurements that, along with the corresponding illumination/viewing geometric parameters, are used to populate the lunar model. Through a series of regressions, these values are developed into an analytic function of observation geometry for each ROLO band.

3.3. The Lunar Disk Reflectance Model

The surface of the Moon exhibits a strong increase in brightness at small phase angles, historically termed the "opposition effect." From recent lunar-orbiting spacecraft observations, the opposition effect is shown to become increasingly strong at phase angles as small as $0°.1$, being stronger over highlands than maria and slightly stronger toward shorter wavelengths (Buratti et al. 1996). There have been a number of efforts to develop physically based models to describe these observations, concluding that the major cause is shadow hiding (Buratti et al. 1996; Hillier 1997) or shadow hiding and coherent backscatter (Hapke 2002), with coherent backscatter being most important for very small phase angles (Helfenstein et al. 1997; Hillier et al. 1999; Shkuratov et al. 1999). Helfenstein et al. (1997) fitted a variety of lunar radiance and irradiance data

TABLE 2

ALEX TABLE CONTENTS

Index	Name	Description
	Integer Values	
0...	LDATE	ROLO Lunar Date of observation
1...	SERIES_NUM	Image series number
2...	CO_ADDS	Number of co-adds
3...	FILTER_ID	ROLO filter identification number
4...	NCHIPS	Number of chips defined in arrays
	Floating-Point Values	
0...	TELE_HOUR	Telescope hour angle (hr)
1...	TELE_RA	Telescope R.A. (hr)
2...	TELE_DEC	Telescope decl. (deg)
3...	TELE_EPOCH	Telescope epoch (yr)
4...	AIR_TEMP	Air temperature ($^{\circ}$C)
5...	WIND_SPEED	Wind speed (m s^{-1})
6...	EXP_TIME	Exposure time (s)
7...	CAM_HEAD_T	Camera head temperature (unconnected) (no data)
8...	WAVELENGTH	Wavelength of filter (μm)
9...	FWHM	Filter FWHM (μm)
10...	EPOCH	Epoch of observation (yr)
11...	ZDIST	Telescope zenith angle (deg)
12...	AZIMUTH	Telescope azimuth, north through east (deg)
13...	RRATE	Motion of target in R.A. (arcsec s^{-1})
14...	DRATE	Motion of target in decl. (arcsec s^{-1})
15...	PHASE	Topocentric phase angle of Moon (deg)
16...	SEMI_DIA	Topocentric semidiameter (deg)
17...	BRI_LIMB	Moon bright limb angle (deg)
18...	POS_AXIS	Moon position axis (deg)
19...	ELAT	Selenographic sub-Earth latitude (deg)
20...	ELON	Selenographic sub-Earth longitude (deg)
21...	SLAT	Selenographic subsolar latitude (deg)
22...	SLON	Selenographic subsolar longitude (deg)
23...	HOUR_ANGLE	Target ephemeris hour angle (hr)
24...	RIGHT_ASCEN	Target ephemeris R.A. (hr)
25...	DECLINATION	Target ephemeris decl. (deg)
26...	SIDEREAL	Sidereal time of exposure (decimal hr)
27...	JULIAN_DATE	Julian date of observation minus 2,450,000
28...	PLANET_DEC	Lunar spin axis decl. in J2000.0 (deg)
29...	PLANET_RA	Lunar spin axis R.A. in J2000.0 (hr)
30...	PLANET_ROT	Lunar prime meridian rotation in J2000.0 (deg)
31...	SC_TARG_X	ROLO telescope to target vector X (km)
32...	SC_TARG_Y	ROLO telescope to target vector Y (km)
33...	SC_TARG_Z	ROLO telescope to target vector Z (km)
34...	SC_SUN_X	ROLO telescope to Sun vector X (km)
35...	SC_SUN_Y	ROLO telescope to Sun vector Y (km)
36...	SC_SUN_Z	ROLO telescope to Sun vector Z (km)
37...	MOONSUM	Sum of lunar disk (DN s^{-1})
38...	MOONERR	Error in sum of lunar disk (fractional)
39...	SKYVAL	Average of sky surrounding Moon (DN s^{-1} pixel^{-1})
40...	SKYERR	Error in SKYVAL (DN s^{-1} pixel^{-1})
41...	EF2_SP1	Constant pixel error term (DN s^{-1} pixel^{-1})
42...	EF2_SP2	Linear pixel error term (fractional)
43...	EF2_SP3	Quadratic pixel error term [(DN s^{-1})$^{-1}$ pixel^{-1}]
44...	CALIBRATION	Radiance calibration factor [W m^{-2} sr^{-1} nm^{-1}(DN s^{-1})$^{-1}$]
45...	CALIBERR	Error in calibration factor (fractional)
46...	EXTINCTION	Extinction correction coefficient
47...	EXTINCTERR	Error in extinction coefficient (fractional)
48–59.....................................	CHIP_AVG_x	Chip averages (DN s^{-1})

TABLE 3
ALEX TABLE CHIPS

		SELENOGRAPHIC LOCATION		ALEX IMAGE			
				LINE RANGE		SAMPLE RANGE	
		Latitude	Longitude				
INDEX	NAME	(deg)	(deg)	Min.	Max.	Min.	Max.
0............	Mare Serenitatus	19.06	20.47	203	205	373	375
1............	East edge	−5.81	69.80	315	317	541	543
2............	North edge	70.46	−16.27	31	33	262	264
3............	South edge	−71.06	−28.64	546	548	245	247
4............	West edge	−2.62	−73.88	300	302	25	27
5............	Aristarchus 3×3	23.30	−47.35	183	185	109	111
6............	Aristarchus 7×7	23.30	−47.35	181	187	107	113
7............	Copernicus	9.48	−20.11	245	247	200	202
8............	Tycho	−43.50	−11.06	468	470	251	253
9............	Highlands	−17.21	20.01	364	366	372	374
10.........	Tycho ray	−37.09	−16.88	445	447	227	229

considered to be acquired at one wavelength and covering phase angles from near $0°$ to $143°$; they concluded that the effective angular half-width for coherent backscatter is near $2°$, and the effective angular half-width for shadow hiding is near $18°$.

We have attempted to fit the ROLO reflectance data using the analytic phase function of Shkuratov et al. (1999), which was derived from physical principles of scattering. Their form (Shkuratov et al. 1999, eq. [31]) is quite complex; the unknowns, in addition to the geometric albedo, are those that enter nonlinearly: the characteristic attenuation scale L of light diffusing in the medium, the formal parameter k "close in some sense to" the limit of the cumulative rms slope of a physical fractal surface, and the radius d characteristic of the volume in which single scattering occurs (roughly the pore radius). Even allowing k and d to vary with wavelength, the minimum mean absolute residual we attained was 4%. We did not attempt to make the nonlinear parameters functions of libration. Using the empirical photometric model of Hillier et al. (1999), which allows for fourth order in phase angle and a single exponential term for the opposition effect, we could attain a mean absolute residual of 2.9%.

In this limited set of trials, we found that fitting physically based models to the extensive ROLO observations yielded residuals considerably larger than the observational noise; current physically based irradiance models do not support the accuracy of the ROLO observations. We have not yet investigated integral phase functions based on Hapke functions (Hapke 1993, p. 455). This is clearly an area for further development.

3.3.1. Model Analytic Form and Derivation of Model Coefficients

ROLO has developed a model of the equivalent reflectance of the entire lunar disk (regardless of illuminated fraction) as a function of geometry. To fit the ROLO observations, we have used an empirically derived analytic form based on the primary geometric variables:

$$\ln A_k = \sum_{i=0}^{3} a_{ik} g^i + \sum_{j=1}^{3} b_{jk} \Phi^{2j-1} + c_1 \theta + c_2 \phi + c_3 \Phi\theta + c_4 \Phi\phi$$
$$+ d_{1k} e^{-g/p_1} + d_{2k} e^{-g/p_2} + d_{3k} \cos[(g-p_3)/p_4], \quad (10)$$

where A_k is the disk-equivalent reflectance, g is the absolute phase angle, θ and ϕ are the selenographic latitude and longi-

tude of the observer, and Φ is the selenographic longitude of the Sun.

The first polynomial represents the basic photometric function dependence on phase angle, disregarding any opposition effect. The second polynomial approximates the dependence on the face of the Moon that is illuminated, primarily representing the distribution of maria and highlands. The four terms with coefficients c_n represent the face of the Moon that is seen (topocentric libration), with a consideration of how that is illuminated. The forms of the last three terms, all nonlinear in g, are strictly empirical; the first two represent the opposition effect, and the last one simply addresses a correlation seen in the irradiance residuals, possibly associated with mare/highland distribution not covered by the second polynomial.

The values of the nonlinear parameters were determined by first fitting the ROLO observations in the traditional least-squares sense using the above form, except that all the nonlinear terms were omitted. Data were constrained to $1°.55 < g < 97°$ (the lower limit is slightly conservative before the onset of eclipse), with the requirement that all data used be part of complete 32 filter sequences. Data points were weighted based on nightly observing conditions. Initially, data for each filter were fitted independently three times. After the first iteration, points with residuals greater than 3 σ of all residuals were removed (typically about a dozen points), and after a second fit, any points with residuals more than 0.25 were removed (typically zero points; the 2130 nm band has about 30 such points). This process leaves about 1200 observations for each filter.

Then, the ∼38,000 residuals from all filters were averaged into 200 uniformly sized bins in phase angle, and these residuals were fitted with the nonlinear terms included, plus an additional linear term that was later dropped. A single exponential term was found inadequate to model the behavior at small phase angles. There is an extended solution curve in the four-dimensional nonlinear parameter space along which the χ^2 term varies negligibly; the solution with widest separation of the two exponential angles was chosen.

All filters were then fitted again with the same process, this time using fixed values for the nonlinear parameters to create the corresponding linear basis functions. Finally, the four coefficients for libration were fixed at their average over wavelength, and all data fitted again.

TABLE 4
ROLO Lunar Irradiance Model Coefficients, Version 311g

|					Coefficient, Term, Name					
Wavelength (nm)	a_0, 1, Constant	a_1, g, Phase 1 (rad^{-1})	a_2, g^2, Phase 2 (rad^{-2})	a_3, g^3, Phase 3 (rad^{-3})	b_1, Φ, SunLon 1 (rad^{-1})	b_2, Φ^3, SunLon 3 (rad^{-3})	b_3, Φ^5, SunLon 5 (rad^{-5})	d_1, e^{-g/p_1}, Exponent 1	d_2, e^{-g/p_2}, Exponent 2	d_3, $\cos[(g-p_3)/p_4]$, Cosine
350.0...............	−2.67511	−1.78539	0.50612	−0.25578	0.03744	0.00981	−0.00322	0.34185	0.01441	−0.01602
355.1...............	−2.71924	−1.74298	0.44523	−0.23315	0.03492	0.01142	−0.00383	0.33875	0.01612	−0.00996
405.0...............	−2.35754	−1.72134	0.40337	−0.21105	0.03505	0.01043	−0.00341	0.35235	−0.03818	−0.00006
412.3...............	−2.34185	−1.74337	0.42156	−0.21512	0.03141	0.01364	−0.00472	0.36591	−0.05902	0.00080
414.4...............	−2.43367	−1.72184	0.43600	−0.22675	0.03474	0.01188	−0.00422	0.35558	−0.03247	−0.00503
441.6...............	−2.31964	−1.72114	0.37286	−0.19304	0.03736	0.01545	−0.00559	0.37935	−0.09562	0.00970
465.8...............	−2.35085	−1.66538	0.41802	−0.22541	0.04274	0.01127	−0.00439	0.33450	−0.02546	−0.00484
475.0...............	−2.28999	−1.63180	0.36193	−0.20381	0.04007	0.01216	−0.00437	0.33024	−0.03131	0.00222
486.9...............	−2.23351	−1.68573	0.37632	−0.19877	0.03881	0.01566	−0.00555	0.36590	−0.08945	0.00678
544.0...............	−2.13864	−1.60613	0.27886	−0.16426	0.03833	0.01189	−0.00390	0.37190	−0.10629	0.01428
549.1...............	−2.10782	−1.66736	0.41697	−0.22026	0.03451	0.01452	−0.00517	0.36814	−0.09815	−0.00000
553.8...............	−2.12504	−1.65970	0.38409	−0.20655	0.04052	0.01009	−0.00388	0.37206	−0.10745	0.00347
665.1...............	−1.88914	−1.58096	0.30477	−0.17908	0.04415	0.00983	−0.00389	0.37141	−0.13514	0.01248
693.1...............	−1.89410	−1.58509	0.28080	−0.16427	0.04429	0.00914	−0.00351	0.39109	−0.17048	0.01754
703.6...............	−1.92103	−1.60151	0.36924	−0.20567	0.04494	0.00987	−0.00386	0.37155	−0.13989	0.00412
745.3...............	−1.86896	−1.57522	0.33712	−0.19415	0.03967	0.01318	−0.00464	0.36888	−0.14828	0.00958
763.7...............	−1.85258	−1.47181	0.14377	−0.11589	0.04435	0.02000	−0.00738	0.39126	−0.16957	0.03053
774.8...............	−1.80271	−1.59357	0.36351	−0.20326	0.04710	0.01196	−0.00476	0.36908	−0.16182	0.00830
865.3...............	−1.74561	−1.58482	0.35009	−0.19569	0.04142	0.01612	−0.00550	0.39200	−0.18837	0.00978
872.6...............	−1.76779	−1.60345	0.37974	−0.20625	0.04645	0.01170	−0.00424	0.39354	−0.19360	0.00568
882.0...............	−1.73011	−1.61156	0.36115	−0.19576	0.04847	0.01065	−0.00404	0.40714	−0.21499	0.01146
928.4...............	−1.75981	−1.45395	0.13780	−0.11254	0.05000	0.01476	−0.00513	0.41900	−0.19963	0.02940
939.3...............	−1.76245	−1.49892	0.07956	−0.07546	0.05461	0.01355	−0.00464	0.47936	−0.29463	0.04706
942.1...............	−1.66473	−1.61875	0.14630	−0.09216	0.04533	0.03010	−0.01166	0.57275	−0.38204	0.04902
1059.5.............	−1.59323	−1.71358	0.50599	−0.25178	0.04906	0.03178	−0.01138	0.48160	−0.29486	0.00116
1243.2.............	−1.53594	−1.55214	0.31479	−0.18178	0.03965	0.03009	−0.01123	0.49040	−0.30970	0.01237
1538.7.............	−1.33802	−1.46208	0.15784	−0.11712	0.04674	0.01471	−0.00656	0.53831	−0.38432	0.03473
1633.6.............	−1.34567	−1.46057	0.23813	−0.15494	0.03883	0.02280	−0.00877	0.54393	−0.37182	0.01845
1981.5.............	−1.26203	−1.25138	−0.06569	−0.04005	0.04157	0.02036	−0.00772	0.49099	−0.36092	0.04707
2126.3.............	−1.18946	−2.55069	2.10026	−0.87285	0.03819	−0.00685	−0.00200	0.29239	−0.34784	−0.13444
2250.9.............	−1.04232	−1.46809	0.43817	−0.24632	0.04893	0.00617	−0.00259	0.38154	−0.28937	−0.01110
2383.6.............	−1.08403	−1.31032	0.20323	−0.15863	0.05955	−0.00940	0.00083	0.36134	−0.28408	0.01010
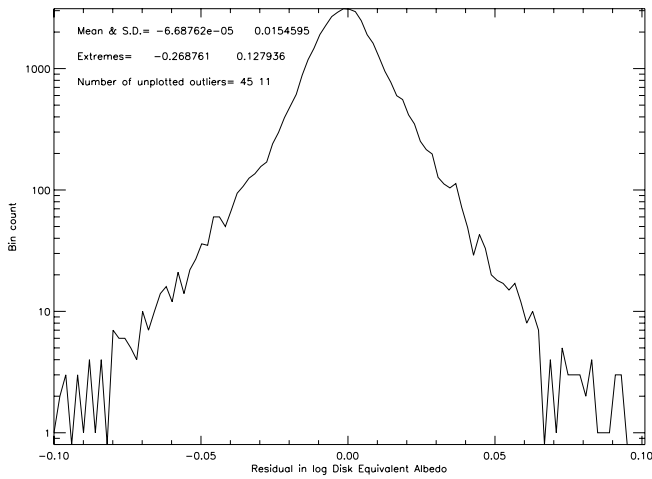
FIG. 5.—Histogram of the residuals for model 311g for all irradiance data used in the fit. The residuals are roughly normally distributed, with a standard deviation of 0.015; the density of residuals drops 2 orders of magnitude by 0.05. There are 38,232 points total, with 45 unplotted outliers below the plot limit and 11 above.

This process yields eight values that are constant over wavelength (four for libration and the four nonlinear parameters) and 10 additional values for each filter, for a total of 328 coefficients. The wavelength-dependent coefficients for the current model version, called 311g, are listed in Table 4; the eight constant 311g coefficients are

$$c_1 = 0.00034115, \quad c_2 = -0.0013425, \quad c_3 = 0.00095906,$$
$$c_4 = 0.00066229, \quad p_1 = 4.06054, \quad p_2 = 12.8802,$$
$$p_3 = -30.5858, \quad p_4 = 16.7498. \quad (11)$$

The mean absolute residual over all observations fitted is 0.0096 in the natural logarithm of reflectance. A histogram of the residual distribution is shown in Figure 5. No significant relation has been found between these residuals and any of the geometric parameters, including the selenographic latitude of the Sun.

4. LUNAR MODEL PERFORMANCE

4.1. *Magnitude of Lunar Variation (Libration and Phase)*

Example values of each model coefficient or parameter, averaged over all ROLO bands, are given in Table 5. These values should not be used to compute lunar albedo at a particular wavelength but are given here to show the relative importance of each term. The "Effect" column in Table 5 gives the magnitude of the change in $\ln A$ for each term over the full range of its variables. Modeling based on more than 6 years of observations indicates that the extreme effects of libration could exceed 7% over a full Saros cycle, of which the first two terms (without Φ) constitute about half. These magnitudes are similar to estimates made by integrating the albedo of appropriate faces of the Moon using a digital map constructed from *Clementine* data (Kieffer & Anderson 1998).

An example lunar phase function is given in Figure 6 for the ROLO 555 nm band. This plot shows the fit residuals as vertical line segments joining the fitted reflectance function to 1234 data points. A few of these are outlier points eliminated in later steps of the fitting process.

Among the lunar reflectance properties predicted by the model is the change of color with phase. It has long been reported that the Moon appears redder away from full Moon (e.g., Lane & Irvine 1973). This is clearly shown by computing model reflectance spectra at various phase angles and normalizing to a spectrum near full Moon, as shown in Figure 7. The "reddening" of the Moon is stronger at long wavelengths for the waxing Moon, and in the blue for the waning Moon.

4.2. *Adjusting the Absolute Scale versus Wavelength*

The model produced by direct fitting of the ROLO observations using the star-based nightly calibration (§ 2.3.2) yields reflectance spectra that have modest excursions in wavelength between bands, whereas the reflectance spectrum of the Moon has only weak, broad features (McCord & Johnson 1970; Lane

TABLE 5
EXAMPLE LUNAR IRRADIANCE MODEL COEFFICIENTS

Symbol	Term	Name	Value	Effect
a_0	g^0	Constant	-1.889	
a_1	g^1	Phase 1	-1.627 (rad^{-1})	2.811
a_2	g^2	Phase 2	0.438 (rad^{-2})	1.309
a_3	g^3	Phase 3	-0.235 (rad^{-3})	1.212
b_1	Φ^1	SunLon 1	0.0425 (rad^{-1})	0.147
b_2	Φ^3	SunLon 3	0.0132 (rad^{-3})	0.137
b_3	Φ^5	SunLon 5	-0.005 (rad^{-5})	0.157
c_1	θ	Libr X	0.0003^* (deg^{-1})	0.005
c_2	ϕ	Libr Y	-0.0013^* (deg^{-1})	0.028
c_3	$\Phi\theta$	SunLon×LibX	0.0010^* (deg^{-1} rad^{-1})	0.026
c_4	$\Phi\phi$	SunLon×LibY	0.0006^* (deg^{-1} rad^{-1})	0.017
d_1	e^{-g/p_1}	Exponent 1	0.389	0.264
d_2	e^{-g/p_2}	Exponent 2	-0.148	0.130
d_3	$\cos[(g-p_3)/p_4]$	Cosine	-0.0035	0.004
p_1		Exponent 1	4.06^* (deg)	
p_2		Exponent 2	12.88^* (deg)	
p_3		Phase	-30.59^* (deg)	
p_4		Period	16.75^* (deg)	

NOTE.—An asterisk indicates that the value is constant for all wavelengths.
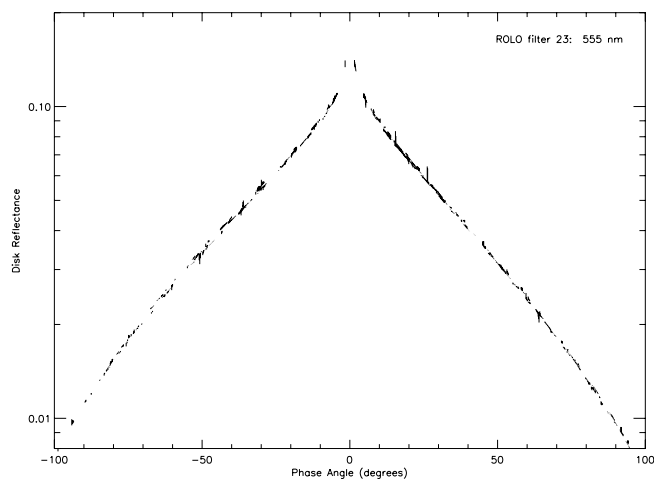
FIG. 6.—Lunar disk reflectance vs. phase angle. The plot symbols are vertical lines drawn between the ROLO data and the model fit. Negative signed phase angles are used to indicate waxing lunar phases.

& Irvine 1973; McCord et al. 1981; Lucey et al. 1986). An adjustment to the model absolute scale for each wavelength was developed from laboratory reflectance spectra of returned *Apollo* samples of soil[4] (*Apollo 16* sample 62231; Pieters 1999) and breccia (*Apollo 16* sample 67455; Pieters & Mustard 1988). A composite spectrum (95% soil) was scaled $[A' = (a + b\lambda)A]$ to fit the ROLO model reflectance spectrum for $g = 7°$, $\Phi = 7°$, $\theta = 0$, and $\phi = 0$ (see Fig. 8). The adjustment factor for each ROLO filter is that required to match the ROLO model to the scaled *Apollo* spectrum; the average correction is 3.5%.

Because lunar maria exhibit greater depth for the FeO bands near 950 and 1900 nm than do the highlands (McCord et al. 1981), the *Apollo 16* soil sample may underestimate the band

---

[4] This *Apollo* soil spectrum is available at http://www.planetary.brown.edu/pds/AP62231.html.
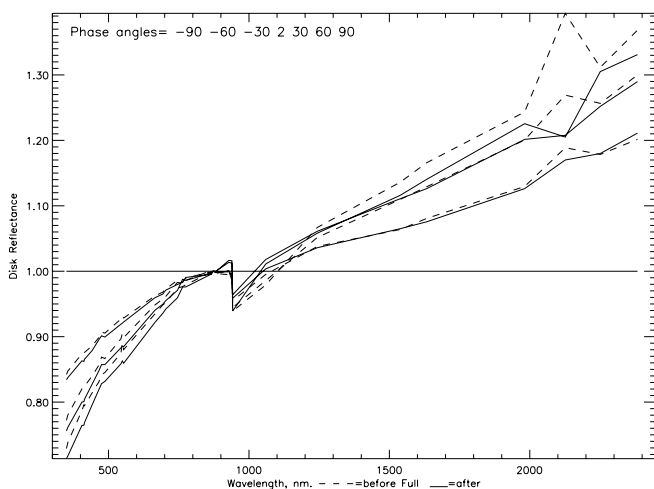
FIG. 7.—Change of lunar color with phase angle. Disk reflectance is normalized to 873 nm and 2° phase. Phase angles are 30°, 60°, and 90°. Dashed lines are waxing lunar phases, and solid lines are waning. Libration is set to zero. The phase color effect is stronger after full Moon at shorter wavelengths and stronger before full Moon at longer wavelengths. The offset at 930 nm is the change between the VNIR and SWIR systems. Values at 2130 nm show anomalous deviations; we expect the true lunar behavior to be smooth with wavelength.
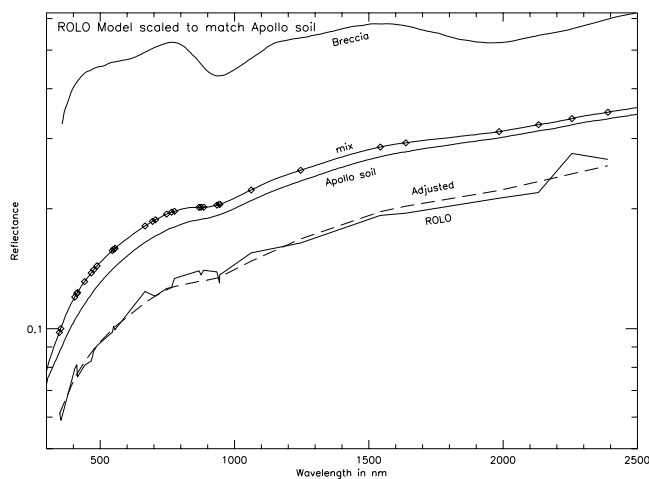
FIG. 8.—Adjustment to the ROLO model reflectance using *Apollo* spectra. The three upper curves are a returned *Apollo* soil sample at 5 nm resolution (*lower solid line*; Pieters 1999), a lunar breccia sample (*upper solid line*; Pieters & Mustard 1988), and a mix with 5% breccia with convolution over the ROLO bands (*diamonds*). The lower jagged line is the unadjusted ROLO model lunar spectrum for 7° phase angle and zero libration. The dashed line is the *Apollo* representative (mixed) spectrum scaled by $a + b\lambda$ to best fit the ROLO spectrum, yielding the 311g model.

strength for the integrated Moon. Thus, the adjustment used here may cause a few percent overestimate in the lunar irradiance near 950 and 1900 nm. In addition, the soil sample spectrum we used was measured at a phase angle of 30° versus our 7°; formulating the adjustment as above against the average of the lunar model at +30° and −30° phase angle would increase the ROLO model by up to 4% between 440 and 700 nm.

4.3. *Uncertainties*

The ROLO project goals for lunar calibration of spacecraft call for overall uncertainties below 1% relative and ∼2.5% absolute (Kieffer & Wildey 1996); the former has been demonstrated for modeling the lunar photometric behavior and for spacecraft instrument response trending (Barnes et al. 2004). Reduction of uncertainties has driven the development approaches for the ROLO methods for absolute calibration and atmospheric extinction correction, including stellar target selection and frequency, and the analytic form of the irradiance model.

4.3.1. *Image Processing*

Statistics-based experimental errors are generated at all stages of the data reduction from raw images through the integration to irradiance. Table 6 lists several of the processing steps, with sample uncertainty values averaged over a typical VNIR 23 band sequence, given as percent relative. Further analysis of ROLO image and irradiance data reveals actual errors in excess of the statistics-generated values; these are given in the column "Practical Estimates." Detector-related uncertainties (bias, dark current, flat-fielding) are generated from statistical sampling of pixel values; uncertainties in derived quantities such as disk centering are developed from formal error analyses, propagating the image data uncertainties through the computations. ANSI floating-point single and double precision is utilized throughout the reduction routines; the table entries have been rounded.

4.3.2. *Atmospheric Correction Algorithm*

The gradient minimization routine used to fit the stellar extinction measurements iterates to a best-fit solution for the

	Relative Uncertainty (%)	
Processing Step	Statistics-based	Practical Estimates
Bias correction........................	0.0368	
Dark current correction..........	0.0846	
Image flat-fielding..................	2.23×10^{-4}	
Lunar disk centering..............	0.0750	0.4 ($\sim$1 pixel)
Sum to irradiance...................	0.00432	0.2
Atmospheric correction*........	0.743	0.7
Radiance calibration*.............	0.216	3.1

Note.—An asterisk indicates that the value for the step is exclusive of absolute scale.

abundances of the seven atmospheric absorbing species. The spectral accuracy of the lunar irradiance model depends critically on an accurate specification of the atmospheric transmission over ROLO. We have identified some areas in need of further study in order to reduce uncertainties in the extinction determinations. The transmission spectra for a number of the aerosol components are very similar (see Fig. 3), which can lead to problems with the matrix inversion solutions. Therefore, the complement of aerosols chosen is being reevaluated on the basis of the fitted abundance results. The aerosol spectra generated by MODTRAN, version 3.7, were found to have discontinuous, cusplike interpolations between data points; a replacement interpolation routine has been implemented for ROLO work.

Although the majority of observation time has been dedicated to stellar extinction measurements, the range of zenith angles covered in a night can be limited, and not higher than $60°$ except for dedicated calibration observations. To better constrain the nightly extinction fit, a table of exoatmospheric stellar irradiances has been generated from the collective set of observations and is used in conjunction with a time-dependent term for nightly variations in instrument gain. There is also an accommodation for the long-term degradation of the optical surfaces. Separate analysis of the nightly extinction calculations has shown that the zero air mass constraint is necessary to obtain consistent extinction results. However, atmospheric correction based on the given air-mass coverage may be a fundamental limitation to the absolute accuracy achievable with the ROLO data set.

4.3.3. Absolute Scale

Uncertainty in the Vega-based radiance calibration can be no less than that in the absolute flux measurements on which it is based. Hayes (1985) cites a measurement uncertainty of 1.5% for the absolute flux at 555.6 nm, the scaling point for the visible-wavelength flux spectrum. The reported experimental error for the IR measurements of Strecker et al. (1979) is $\sim$4% absolute. Both sets of absolute flux data rely on an assumed energy distribution for Vega.

The method for scaling the Kurucz model spectrum to the absolute flux distributions follows that used by Gray (1998) for calibrating the Strömgren uvby bands. Gray estimated the random errors introduced by this technique to be $\sim$1% or less. Calculation of the Vega absolute fluxes in the ROLO bands involves convolution with the band spectral response functions, including the modeled transmission wavelength shift for interference filters with off-normal incidence inherent in the Cassegrain optical feed. The RSR for several ROLO bands has

been measured through the full optical system using the ROLO collimated light source (§ 2.3.2) fed by tunable lasers from the NIST field-deployable SIRCUS facility (Brown et al. 2000). Preliminary results show bandpass shifts of up to several nanometers from the normal-incidence transmission functions, providing a check on the wavelength shift model.

An additional uncertainty, as yet unquantified, concerns the validity of using a stellar (i.e., point) light source to calibrate extended radiance images such as the lunar disk or ground scenes from satellites. We are aware of past experimental investigations into this effect but have found no published report of a quantitative correction. This is an additional area under study as part of the ROLO/NIST field calibration effort.

4.3.4. Irradiance Data and Model Predictions

The circular region used to integrate a lunar disk image to irradiance is defined by fitting $160°$ of arc to the bright limb, defined as the inflection point of the transition from lunar surface to sky background. This fit is iterated until the computed center line/sample positions change by less than 10^{-4} pixels. Statistics on the computed limb radius, sampled $1.35 \times$(radius in pixels) times, are generated for each band; an average is given in Table 6.

Uncertainty in the summation to irradiance (eq. [5]) is derived from the cumulative error in determining the detector counts corresponding to photons from the Moon. This accounts for all detector artifact corrections and calibration uncertainties and combines the uncertainty of the sky background subtraction. Summed irradiances are corrected for point-spread effects in the ground-based lunar observations; an analytic correction was developed from radial profiles of the sky background for a selected set of lunar images acquired over the ROLO operational range of phase angles.

The analytic form of the disk reflectance model, equation (10), was developed with the goal of fitting the observational data in each band to the extent that there is no correlation within the residuals. A histogram of the residuals, Figure 5, shows the effectiveness of the multiple-iteration process described in § 3.3.1; less than 1% of all residuals are higher than 5% deviation. This is a measure of the lunar model precision extending over the range of the geometric variables. However, it says nothing of accuracy on an absolute scale.

5. APPLICATION TO SPACECRAFT IMAGING INSTRUMENTS

To apply the ROLO lunar model, the circumstances of a spacecraft observation must be known, along with the RSR of each spacecraft band. From the latter, the effective wavelength for the Moon is computed using the definition of equation (1) with the lunar irradiance spectrum at the reference angular geometry we have adopted: a $7°$ phase angle and zero libration.

The lunar reflectance model (eq. [10]) is evaluated for the angular geometry of each spacecraft observation using the fit coefficients for each ROLO band; these values are interpolated to the spacecraft band effective wavelength using linear interpolation, with an additional shape factor that preserves the detailed shape of the Apollo reference spectrum between the ROLO observation wavelengths. The resulting disk reflectances are converted to irradiance using the average in-band solar irradiance derived by convolution of the instrument spectral response with the high-resolution solar spectrum (eq. [9]) and the relation in equation (8). These model irradiances at standard distances are then corrected to the actual distances for each observation using the relation in equation (7).

5.1. *Spacecraft Observations of the Moon*

Several instruments have now viewed the Moon while in orbit, and observations have been compared with the ROLO model. Typically, the spacecraft will execute a pitch maneuver while in the Earth's shadow to scan past the Moon. For instruments in a Landsat-like orbit (705 km altitude), the Moon's diameter corresponds to roughly 6.3 km on the ground, and lunar image acquisition takes only a few seconds. The lunar image is processed to radiance in the same fashion as standard image data products, and the radiance of pixels on the Moon is summed and multiplied by the solid angle of a pixel to obtain the equivalent lunar irradiance. The apparent angular velocity of the Moon relative to the standard angular velocity of the Earth in normal viewing configuration, the "oversample factor," must be determined in some fashion, as this factor enters linearly into the calibration. For some spacecraft, this can be determined from attitude telemetry; for others, it must be determined from the apparent size of the Moon in the pitch rate direction in the image itself. In the latter case, for instruments with low resolution (e.g., SeaWiFS with 1 km pixels and a ~1% uncertainty in the oversample factor), this can limit the accuracy of the comparison.

The spacecraft instrument team supplies to ROLO the spacecraft location and time at the midpoint of the lunar observation, along with the apparent size of the Moon in the scan direction. The ROLO team then computes the relative positions of the spacecraft and the Sun in selenographic coordinates using the high-precision ephemeris of the Moon and planets (Standish 1990) and the IAU orientation of the Moon (Davies et al. 1992). The lunar irradiance model is computed for this geometry and corrected for the actual Moon-Sun and Moon-spacecraft distances for comparison with the spacecraft observation.

5.2. *Results for Several Spacecraft*

The number of observations made by instruments in orbit ranges from 1 for the EOS *Terra* nadir-viewing instruments to more than 70 for SeaWiFS. The *Terra* and *Aqua* MODIS instruments also have a space-view port through which the Moon can be viewed at phase angle $+55°$ and $-55°$, respectively (although phase angle is a strictly positive quantity, negative values are used by ROLO to distinguish illumination geometries before full Moon). Figure 9 shows averages over all comparisons for each of the participating instruments. The discrepancy between instruments is up to about 8% in the silicon CCD region (<1000 nm). Although the absolute scale of the lunar irradiance model is uncertain by several percent, the comparison between similar wavelength bands in different instruments is probably better than 1%. Figure 9 suggests a fundamental inconsistency in radiometric scales of the standard data products from these instruments. For the Hyperion imaging spectrometer, there are significant rapid spectral variations, as well as strong inverted features near 1400 and 1900 nm that probably result from water vapor absorption in the optical path during laboratory calibration. The MODIS "land" bands at 902, 935, and 940 nm are considerably higher than for other instruments. MODIS calibrations from the *Terra* nadir view (made during the single *Terra* lunar attitude maneuver) and the *Terra* and *Aqua* space-view port observations (26 and 20 observations, respectively) have similar spectral shapes and agree to within about 1%, although they were acquired over a $110°$ range of phase angles. Hyperion has made observations at phase angles from $6°$ to $85°$, and despite the variation in lunar irradi-
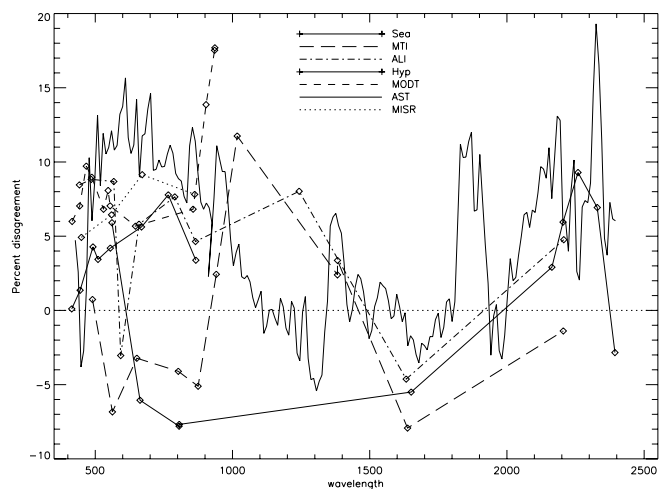

Fig. 9.—Lunar calibration of several on-orbit imaging instruments using the 311g model. The ordinate is the ratio of the spacecraft-reported irradiance to that of the ROLO model, expressed as a percentage difference from unity. The plot symbols represent effective wavelengths for a lunar spectrum in the instrument bands: (Sea) SeaWiFS on *SeaStar*; (MTI) *Multiband Thermal Imager* (a Department of Energy spacecraft); (ALI) Advanced Land Imager on *EO-1*; (Hyp) Hyperion on *EO-1*; (MODT) MODIS on *Terra*; (AST) ASTER on *Terra*; (MISR) Multiangle Imaging Spectroradiometer on *Terra*.

ance of nearly an order of magnitude between quarter phase and near full Moon, the calibrations agree to within a few percent.

The SeaWiFS results are an average of 70 observations, with each of the eight instrument bands having been fitted with a smooth decay in responsivity before comparison with the Moon (Barnes et al. 2004). The temporal trends in the SeaWiFS comparisons show $\sim\pm0.5\%$ variations, strongly correlated between bands and attributed to poor knowledge of the oversample factor (see § 4). When this correlated variation is removed by applying a single scaling factor to all bands for each observation, the comparison residuals are about 0.1%.

6. CONCLUSIONS

An observational program designed to determine the variation and scale of lunar brightness with high precision was carried out for more than 6 years. Much of the observing time was assigned to stellar measurements to determine atmospheric extinction. Over 80,000 lunar images and several hundred thousand stellar images were acquired, most of which have been processed to determine time-dependent instrument response and atmospheric spectral extinction and ultimately to develop a photometric model of lunar irradiance at 32 wavelengths. The mean absolute residuals from fitting hundreds of observations in each band are just under 1%. Model outputs include a scaling factor to match the spectral reflectance characteristics of returned lunar surface samples.

Although the lunar reflectance model can be improved through additional observations by filling in the four-dimensional space defined by its independent variables, we believe that the 1% residual level may not be significantly reduced. The consistency of the model results in comparing spacecraft observations at diverse geometries exceeds the level of the data fit residuals by an order of magnitude. We assign the cause of these residuals primarily to putative $1–10$ km scale variations of atmospheric opacity that move over the observatory through the night. Multidirectional, simultaneous measurements of many

standard stars would be required to quantify these rapid extinction fluctuations.

This work has demonstrated that the lunar spectral irradiance can be modeled with a precision that enables a significant advancement in on-orbit monitoring of spacecraft instrument performance. The most extensive set of spacecraft lunar observations, the 6 year record of SeaWiFS, suggests that instrument response trending can be determined approaching the 0.1% level on a monthly basis over any longer time period. This level of long-term stability just meets the goals for radiometric calibration of decade-scale climate observations set for the upcoming *National Polar-orbiting Operational Environmental Satellite System* (Bingham et al. 2001). However, this level of precision indicates that it will be useful to incorporate treatment of the variation in solar irradiance, which is at this level, to generate appropriate lunar irradiances using the lunar disk reflectance model.

REFERENCES

Alhajjah, A., Pandey, D. K., Paden, J., Priestley, K. J., Lee, R. B., Wilson, R. S., & Thomas, S. 2004, Proc. SPIE, 5232, 604
Anderson, J. M., Becker, K. J., Kieffer, H. H., & Dodd, D. N. 1999, PASP, 111, 737
Anderson, J. M., & Kieffer, H. H. 1999, in New Views of the Moon II: Understanding the Moon through the Integration of Diverse Datasets, ed. L. Gaddis & C. K. Shearer (Houston: LPI), 2
Anderson, J. M., Kieffer, H. H., & Becker, K. J. 2001, Proc. SPIE, 4169, 248
Barnes, R. A., Eplee, R. E., Jr., Patt, F. S., Kieffer, H. H., Stone, T. C., Meister, G., Butler, J. J., & McClain, C. R. 2004, Appl. Opt., 43, 5838
Barnes, R. A., Eplee, R. E., Jr., Schmidt, G. M., Patt, F. S., & McClain, C. R. 2001, Appl. Opt., 40, 6682
Berk, A., Bernstein, L. S., & Robertson, D. C. 1989, MODTRAN: A Moderate Resolution Model for LOWTRAN 7 (Tech. Rep. GL-TR-89-0122; Hanscom: Phillips Lab.)
Bingham, G., et al. 2001, National Polar-orbiting Operational Environmental Satellite System [NPOESS] Preparatory Project [NPP] Calibration and Product Validation Plan, ver. 11 (Greenbelt: GSFC), http://jointmission.gsfc.nasa.gov/science/Calibration.html
Brown, S. W., Eppeldauer, G. P., & Lykke, K. R. 2000, Metrologia, 37, 579
Bruegge, C. J., Diner, D. J., & Duval, V. G. 1996, J. Atmos. Oceanic Tech., 13, 286
Buratti, B. J., Hillier, J. K., & Wang, M. 1996, Icarus, 124, 490
Castelli, F., & Kurucz, R. L. 1994, A&A, 281, 817
Davies, M. E., et al. 1992, Celestial Mech. Dyn. Astron., 53, 377
Dollfus, A. 1961, Polarization Studies of Planets (Chicago: Univ. Chicago Press)
———. 1962, The Polarization of Moonlight (London: Academic)
———. 1998, Icarus, 136, 69
Dollfus, A., & Bowell, E. 1971, A&A, 10, 29
Folkman, M. A., Pearlman, J., Liao, L. B., & Jarecke, P. J. 2001, Proc. SPIE, 4151, 40
Fröhlich, C. 2000, Space Sci. Rev., 94, 15
Gellman, D. I., Biggar, S. F., Dinguirard, M. C., Henry, P. J., Moran, M. S., Thome, K. J., & Slater, P. N. 1993, Proc. SPIE, 1938, 118
Gray, R. O. 1998, AJ, 116, 482
Guenther, B., et al. 1996, J. Atmos. Oceanic Tech., 13, 274
Hapke, B. 2002, Icarus, 157, 523
Hapke, B. W. 1993, Theory of Reflectance and Emittance Spectroscopy (Cambridge: Cambridge Univ. Press)

Hayes, D. S. 1985, in IAU Symp. 111, Calibration of Fundamental Stellar Quantities, ed. D. S. Hayes, L. E. Pasinetti, & A. G. Davis Phillip (Dordrecht: Reidel), 225
Hayes, D. S., & Latham, D. W. 1975, ApJ, 197, 593
Helfenstein, P., Veverka, J., & Hillier, J. 1997, Icarus, 128, 2
Hillier, J., Buratti, B., & Hill, K. 1999, Icarus, 141, 205
Hillier, J. K. 1997, Icarus, 128, 15
Kieffer, H. H. 1997, Icarus, 130, 323
Kieffer, H. H., & Anderson, J. A. 1998, Proc. SPIE, 3498, 325
Kieffer, H. H., Anderson, J. M., & Becker, K. J. 1999, Proc. SPIE, 3870, 193
Kieffer, H. H., Jarecke, P., & Pearlman, J. 2002, Proc. SPIE, 4480, 247
Kieffer, H. H., & Wildey, R. L. 1985, Photogramm. Eng. Remote Sensing, 51, 1391
———. 1996, J. Atmos. Oceanic Tech., 13, 360
Lane, A. P., & Irvine, W. M. 1973, AJ, 78, 267
Lucey, P. G., Hawke, B. R., McCord, T. B., Pieters, C. M., & Head, J. W. 1986, J. Geophys. Res., 91, 344
Lyot, B. 1929, Ann. Obs. Meudon, 8, 1
McCord, T. B., Clark, R. N., Hawke, B. R., McFadden, L. A., Owensby, P. D., & Pieters, C. M. 1981, J. Geophys. Res., 86, 10883
McCord, T. B., & Johnson, T. V. 1970, Science, 169, 855
Ohring, G., Wielicki, B., Spencer, R., Emery, W., & Datla, R. 2004, CD-ROM, Satellite Instrument Calibration for Measuring Global Climate Change (Boulder: NIST)
Pieters, C. M. 1999, in New Views of the Moon II: Understanding the Moon through the Integration of Diverse Datasets, ed. L. Gaddis & C. K. Shearer (Houston: LPI), 47
Pieters, C. M., & Mustard, J. F. 1988, Remote Sensing Environ., 24, 151
Pugacheva, S. G., Novikov, V. V., & Shevchenko, V. V. 1993, Astron. Vestnik, 27, 47
Shkuratov, Y. G., Kreslavsky, M. A., Ovcharenko, A. A., Stankevich, D. G., Zubko, E. S., Pieters, C., & Arnold, G. 1999, Icarus, 141, 132
Standish, E. M. 1990, A&A, 233, 252
Stone, T. C., & Kieffer, H. H. 2002, Proc. SPIE, 4814, 211
Stone, T. C., Kieffer, H. H., & Anderson, J. M. 2002, Proc. SPIE, 4483, 165
Strecker, D. W., Erickson, E. F., & Witteborn, F. C. 1979, ApJS, 41, 501
Umov, N. 1905, Phys. Zeit., 6, 674
Wehrli, C. 1986, Spectral Solar Irradiance Data (WMO ITD 149; Geneva: WMO)